International Journal of Infrared and Millimeter Waves, Vol. 24, No. 8, August 2003 (© 2003)

THERMAL BEHAVIOR OF AMORPHOUS SILICON THIN FILM TRANSISTOR AND ITS APPLICATION TO MICROMACHINED UNCOOLED INFRARED SENSORS

Liang Dong, Ruifeng Yue, and Litian Liu

Institute of Microelectronics
Tsinghua University
Beijing 100084, China
Email: dongliang99@mails.tsinghua.edu.cn

Received May 30, 2003

ABSTRACT

This work reports a new uncooled infrared sensor based on amorphous silicon thin film transistors (a-Si TFTs). The temperature coefficient of channel current (TCC) of the a-Si TFT is given. Analysis shows that the a-Si TFT working in the saturation region is preferred for the sensitive element with a TCC value of 3.8-6.0 %/K. The a-Si TFT is placed on a suspended microbridge to reduce the thermal conductance by using micro-electro-mechanical system (MEMS) technology. The a-Si TFT-based IR sensor with a monolithic architecture is fabricated. Preliminary experimental results show that a responsivity of 40.8 *k*V/W, a thermal response time of 5.5 *m*s and a NETD of 90 *m*K are achieved.

Key words: uncooled IR sensors, a-Si TFT, MEMS, porous silicon

1. INTRODUCTION

Infrared (IR) detection is of great importance to a number of civilian and military applications ranging from night vision, thermal imaging, biomedical diagnostics, and fire detection. IR sensors can be in general classified into two groups: photon type and thermal type. The photon IR sensors are based on the photoconductive or photovoltaic effect. They are usually cooled to the cryogenic temperature of liquid nitrogen or of liquid helium to suppress the thermal noise from the detection materials that are typically low-bandgap semiconductors.

0195-9271/03/0800-1351/0 © 2003 Plenum Publishing Corporation

They typically have a low noise-equivalent temperature difference (NETD) of 1-20 *m*K and a short response time of less than 1 *m*s, but the indispensable cooling systems have made the IR systems expensive, of heavy-weight, and of large volume. In addition, the photon IR sensors are wavelength selective, and fail to extend to far IR region (8-14 μm). Recently, advances in micro-electro-mechanical systems (MEMS) technology have led to the development of the highly sensitive thermal sensors that can operate as uncooled IR sensors. The operation of the thermal sensors is based on conversion of the IR radiation energy into heat and then into a measurable electrical signal. Since the thermal sensors rely on the temperature changes of the temperature-sensitive element due to the IR absorption rather than on the photo-excitation of carriers, they can operate at room temperature with little wavelength dependence of the response over a wide IR spectrum range. The elimination of expensive cooling system and the feature of relatively flat broadband spectral response can make the IR systems compact, inexpensive and versatile, and thus meet commercial requirements.

Presently, there are several kinds of available uncooled IR sensors, including bolometers of either the resistive [1] or dielectric type [2], pyroelectric [3], thermopile [4], opto-mechanical [5] and mechanical resonance based sensors [6]. Each of these uncooled IR sensors can be modeled as a temperature-sensitive element of thermal capacitance connected to a bulk substrate serving as an infinite heat sink through a thermal conductance [7]. In order to maximize the temperature increase, the sensitive element must be thermally isolated from its surroundings. The use of micromachining techniques makes it possible to fabricate a suspended microbridge where the sensitive element is placed, to minimize the heat loss [8].

Amorphous silicon thin film transistors (a-Si TFTs) have been widely used as the switching components in active matrix liquid crystal displays, X-ray imagers and printing heads. However, the thermal characteristics of a-Si TFTs have little been exploited for the thermal sensors. In this paper, we present a new micromachined uncooled IR sensor based on a-Si TFTs. An important reason that the a-Si TFT is useful for IR detections is that it processes a sensitive temperature dependence of channel current. Apart from this, the a-Si TFT can be processed below 350 °C by using standard integrated circuit (IC) processing without destroying the pre-formed ICs. In consequence, the TFT-based uncooled IR sensors could have a monolithic architecture in view of the integration of the micromachined sensors with the smart electronics.

2. THERMAL BEHAVIOR OF A-SI TFT

In order to evaluate how rapidly the channel current of the a-Si TFT responds to a change in temperature, we introduce the temperature coefficient of channel current (TCC) as a figure-of-merit,

$$\beta = (1/I_d)dI_d/dT, \qquad (1)$$

where I_d is the channel current of the a-Si TFT, and T is the absolute temperature.

The drain current in TFTs can be expressed in essentially as crystalline silicon MOSFETs,

$$I_d = \mu C_i (W/L)[(V_g - V_t)V_d - V_d^2/2],\qquad (2)$$

where μ is the carrier mobility in the channel, C_i is the gate capacitance per unit area, W and L are the gate dimensions, and V_g, V_d, and V_t are the gate voltage, the drain voltage and the threshold voltage, respectively.

In Eq. (2), two important parameters that are sensitive to the temperature are the carrier mobility μ and the threshold voltage V_t. The temperature dependence of the mobility is given by [9]

$$\mu(T) \cong \mu_0 (N_c kT / N_T) \exp(-E_a / kT),\qquad (3)$$

where μ_0 is the extended state electron mobility, N_c is the extended state electron density, N_T is the effective density of band tail states, E_a is the activation energy, and k is the Boltzmann constant.

The threshold voltage V_t depends on the initial charge density n_0 of the a-Si channel region, and is expressed as $V_t \equiv -et_a n_0/C_i$, where t_a is the a-Si thickness [9]. Since at room temperature the initial charge density n_0 in the a-Si is mainly determined by the extended state electron density N_c, n_0 can be expressed as $n_0 = N_c \exp[-(E_c - E_F)/kT]$, where E_c is the conduction band edge energy, and E_F is the Fermi energy. Thus, the temperature dependence of the threshold voltage is given by

$$V_t(T) = -et_a (N_c / C_i) \exp[-(E_c - E_F)/kT].\qquad (4)$$

The expression of TCC (β) can be derived from Eq. (2-4), and is given by

$$\beta = \left(\frac{1}{T} + \frac{E_a}{kT^2}\right) - \frac{V_t}{(V_g - V_t) - V_d/2} \frac{(E_c - E_F)}{kT^2}.\qquad (5)$$

In Eq. (5), the first part represents the temperature coefficient of the carrier mobility, $\alpha = (1/\mu)d\mu/dT$, which is a positive value, while in the second part (not including the minus sign) the item of $V_t(E_c - E_F)/kT^2$ represents the temperature coefficient of the threshold voltage, $\gamma = (1/V_t)(dV_t/dT)$, which is a negative value. It is indicated that both the carrier mobility shift and the threshold voltage shift can contribute to the large TCC value. It is interesting to point out that as the temperature increases, the carrier mobility of the a-Si channel region increases because of the thermal activation of carriers at room temperature, which is essentially different from that of the crystalline silicon in MOSFETs.

The a-Si TFT under study is of n type and of inverted-staggered gate structure, where silicon nitride (SiN_x) is used as the gate insulator, undoped a-Si as the active layer, and doped a-Si as the source/drain contact layer. The a-Si TFT has the bottom gate electrode. The source/drain electrodes and the gate electrode are on opposite sides of the active layer. The ratio of channel width to length of a fabricated a-Si TFT is 100μm/8μm. Fig.1 shows (a) a schematic structure and (b) an optical microscope image of the inverted-staggered gate structure TFT.

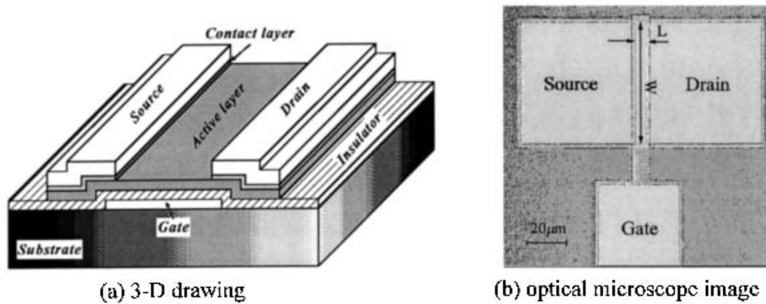

(a) 3-D drawing (b) optical microscope image

Fig. 1. Structure of the inverted-staggered a-Si TFT. (a) 3-D schematic drawing, (b) optical microscope image

The fabrication process of the a-Si TFT is briefly described as follows. Silicon wafers with 500-*nm* thick SiO_2 were used as starting substrates. Initially, a 400-*nm* thick aluminum (Al) was deposited onto the substrates by sputtering and patterned for the gate electrode. Then, 300-*nm* thick SiN_x, 150-*nm* thick undoped a-Si and 30-*nm* thick phosphorus doped n^+ a-Si were deposited consequently without breaking the vacuum at 300 °C by using plasma enhanced chemical vapor deposition (PECVD). After that, 1-μm thick Al layer was deposited on the n^+ a-Si by sputtering and the source/drain electrodes were defined by using photolithography. The n^+ a-Si layer between drain and source electrode was removed by dry etching. Finally, the a-Si TFT was annealed at 350 °C for 40 min in the hydrogen atmosphere.

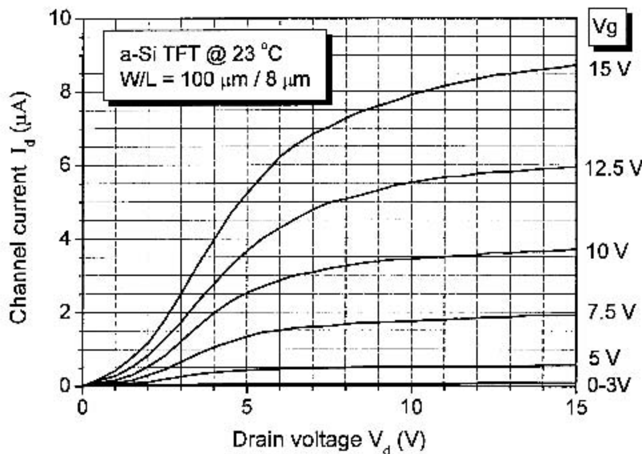

Fig. 2. Channel current vs. drain voltage (I_d-V_d) characteristics of the fabricated a-Si TFT

Fig. 2 shows the channel current vs. drain voltage (I_d-V_d) characteristics measured at various gate voltages (V_g) from 0 to 15 V. The channel current increases with the TFT gate voltage and becomes saturated at a high drain voltage. The threshold voltage of the a-Si TFT is determined to be around 2.7 V from the plot of $I_d^{1/2}$ vs. V_g at V_d=15 V. The carrier mobility (μ) in the saturation region is calculated from Eq. (2), and is approximately 0.45 cm^2/Vs. Thus, the present TFT exhibited a typical transistor characteristic.

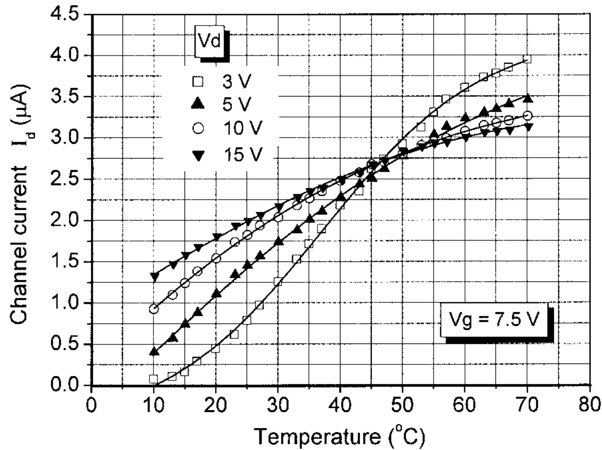

Fig. 3. Channel current vs. temperature (I_d-T) characteristics of the fabricated a-Si TFT

Fig. 3 shows the typical channel current vs. temperature (I_d-T) characteristics measured at V_g=7.5 V and various V_d (3, 5, 10, and 15 V). The temperature ranged from 10 to 70 °C. The channel current increases with the temperature at different rates. The TCC values at 23 °C are calculated from Eq. (1). In case of V_d= 3 V, the a-Si TFT works in the linear region since $0 < V_d < V_g$-V_t is valid. It acts as an a-Si resistor and has a high TCC value of over 8.0 %/K. On the other hand, when the a-Si TFT works in the saturation region since $V_d > V_g$-V_t is valid, the TCC values at V_d= 5, 10, and 15 V are around 6.0, 4.4 and 3.8 %/K, respectively. We believe that the a-Si TFT in the saturation region with a moderate TCC value is preferred for the sensitive element in view of the limitation of thermal noise, since the thermal noise in saturated TFTs is much lower than that in linear-region worked TFTs.

3. A-SI TFT-BASED UNCOOLED IR SENSORS TECHNOLOGY

The cross-sectional view of the a-Si TFT-based uncooled IR sensor is shown in Fig. 4. In this design, the a-Si TFT is placed at a thermally well-isolated microbridge suspending above the silicon substrates, which can limit the heat loss and maximize the temperature increase caused by the absorption of IR radiation. The height of the air cavity between microbridge and substrate is 7.5 μm. The inverted-staggered gate structurized TFT is

preferred, since the bottom gate electrode can serve as a reflecting mirror. Thus, the incident IR radiation will be reflected at the gate metal and be absorbed twice by absorptive materials. For certain spectral bands in region of 8-14 μm, no additional material for enhancing IR absorption is needed, since the SiO_xN_y passivation layer has good IR absorptions due to Si-O bonds (8-10 μm) and Si-N bonds (11-13 μm). Numerical calculations show an absorptance of over 60% can reached in region of 8-14 μm. The IR absorptive performances can be further improved by adjusting the thickness and refractive index of SiO_xN_y layer.

The device integrated with MOS readout electronics has been fabricated by the porous silicon micromachining technique. The fabrication steps are briefly described as follows. The (100)-oriented, 40 Ω·cm, p type wafers were used as starting substrates. Firstly, 7.5-μm deep p^+ regions were selectively formed in the patterned silicon substrates by ion implantation and diffusion. Secondly, the porous silicon sacrificial layer was prepared in the p^+ regions by conventional anodic electrochemical reaction. Thirdly, 100-*nm* SiO_2 and 150-*nm* Si_3N_4 were deposited by low pressure chemical vapor deposition (LPCVD), and then were patterned to protect the porous silicon from being oxidized or cracking during the following processing. Subsequently, MOS readout electronics was fabricated by standard IC processing. Then, the a-Si TFT was fabricated followed by deposition of 800-*nm* thick SiO_xN_y passivation layer. The TFT fabrication details have been described in section 2.2. Finally, the porous silicon sacrificial layer was removed in 5% tetra-methyl-ammonium-hydroxide (TMAH) solution via etching holes to form the thermal isolation structures.

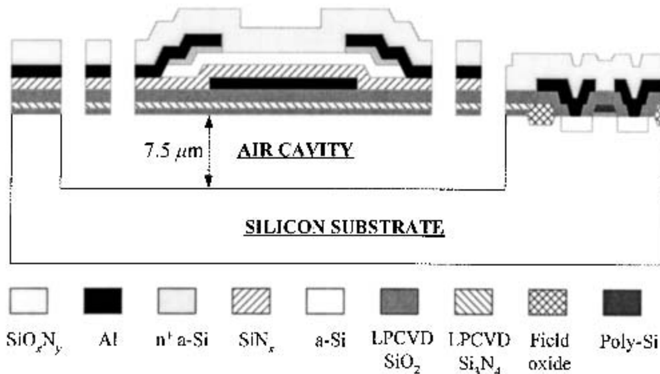

Fig. 4. The cross-sectional view of the a-Si TFT-based uncooled IR sensor

The a-Si TFT-based uncooled IR sensors were arranged in 1×16, 4×4 and 8×8 arrays. We designed several structures with different *W/L* ratio of the TFT varying from 50μm/5μm to 200μm/10μm and different shapes of support legs of the microbridge. The structure of the fabricated pixel is shown in Fig. 5, where the *W/L* ratio of the TFT is 100μm/8μm, and the pixel dimension is 150μm×100μm.

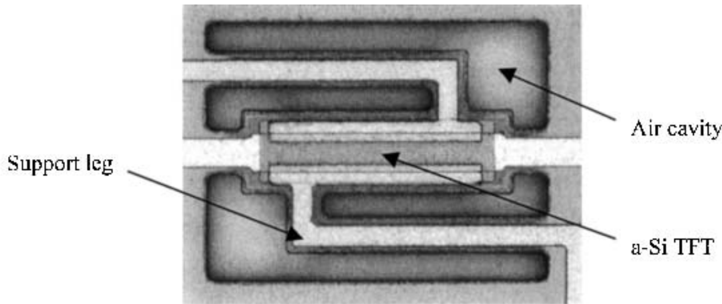

Fig. 5. The optical microscope image of the a-Si TFT-based uncooled IR sensor

4. PRELIMINARY IR CHARACTERIZATION

One of the most significant figure-of-merits of IR sensors is the responsivity, which is defined as the voltage signal generated per unit input IR radiation power on the sensor surface. For our a-Si TFT-based IR sensor, the responsivity R_v can be expressed as

$$R_V = \frac{\eta \beta I_d R_d}{G_{th}\sqrt{1+4\pi^2 f^2 \tau^2}}, \qquad (6)$$

where η is the fraction of incident radiation absorbed, R_d is the channel resistance, G_{th} is the total thermal conductance, f the frequency of the modulation signal, and τ is the thermal time constant defined by the ratio of the sensor's thermal capacitance C_{th} to the thermal conductance G_{th}, C_{th}/G_{th}. In Eq. (6), we can observe that the responsivity is directly proportional to the channel current. It seems that using high drain voltage can ensure high responsivity. However, the higher drain voltage simultaneously results in a reduction of both β and R_d. Furthermore, in case of large-scale 2-D arrays, the total power consumption is considerable if the channel current is not limited.

In order to determine the responsivity, the a-Si TFT IR sensor was connected in series with a low noise battery (constant-voltage source, 10 V) and to an identical a-Si TFT which was on-chip fabricated on the bulk area and acted as the load element. The voltage applied to the gates of both the two TFTs was 7.5 V, and thus they were working in the saturation regions. The device was exposed to the radiation of a calibrated blackbody heated at temperatures ranging from 400 °C to 900 °C. The incident radiation was modulated by a mechanical chopper. The ac voltage signal V_s from the intersection node of the TFT-TFT serially connected circuit was measured using an SR510 lock-in amplifier with a bandwidth of 1 Hz. The noise voltage V_n of the sensor was measured using the same measuring system without blackbody illumination. The test sample is shown in Fig. 5.

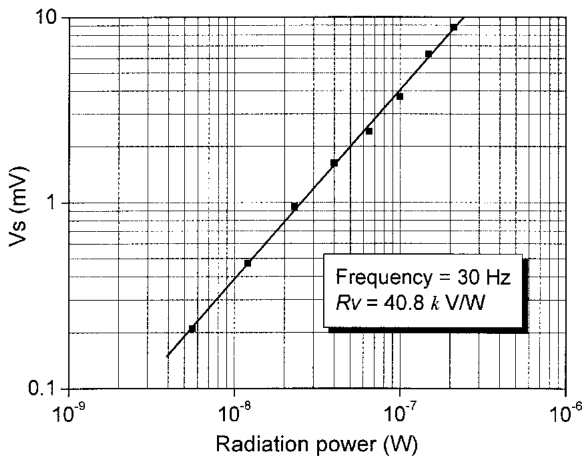

Fig. 6. The voltage signal V_s values as a function of the radiation power

Fig. 6 shows the voltage signal V_s values as a function of the radiation power at a frequency of 30 Hz. The power P is calculated from the equation of $P=\varepsilon\sigma AA_D T^4/(\pi l^2)$, where T is the blackbody temperature, ε is the emissivity, σ is the Stefan-Boltzmann constant (5.67×10^{-8} $Wm^{-2}K^{-4}$), A is the aperture area, A_D is the area of the sensor, and l is the distance from the sensor. It is indicated that the sensor has a linear voltage response with the incident power. The responsivity R_V of 40.8 *k*V/W is obtained from the slope of the best-fit straight of line.

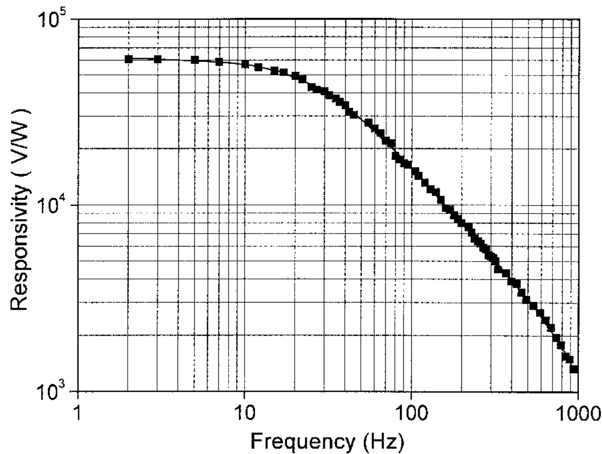

Fig. 7. The voltage responsivity as a function of the frequency

Fig. 7 shows the dependency of the responsivity on frequency of the a-Si TFT-based IR sensor. R_V is almost flat at low frequencies, while decreases at high frequencies in accordance with Eq. (6). The best fits correspond to a thermal time constant of about 5.5 *m*s.

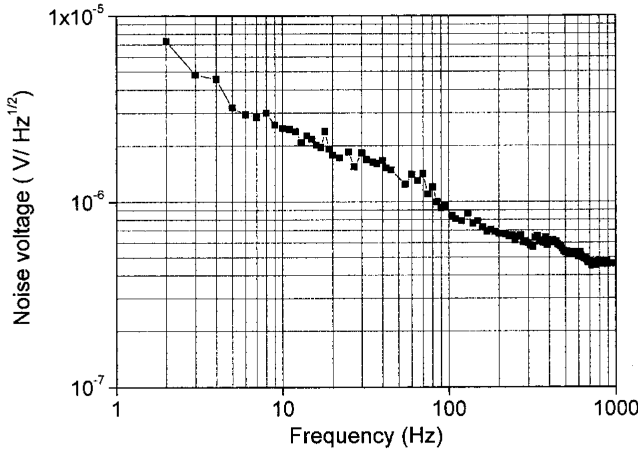

Fig. 8. The noise voltage as a function of the frequency

Fig. 8 shows the dependency of the noise voltage on frequency of the same sensor. The noise voltage distinctly decreases with the frequency until 100 Hz is reached. It may be indicated that the $1/f$ noise dominates over the thermal noise at low frequencies, while the later is the dominant noise at high frequencies. At a frequency of 30 Hz, the total noise voltage is around 1.83 $\mu V/Hz^{1/2}$.

NETD is the other significant figure-of-merit of IR sensors, which is defined as the increase of temperature of the IR source over reference temperature T_{REF} that produces signal-to-noise ratio of 1 in sensors. It can be derived from the measured V_n and R_V through the following equation [10],

$$V_n = R_V [P(T_{REF} + NETD) - P(T_{REF})] = R_V \frac{\varepsilon\sigma}{\pi l^2}[(T_{REF} + NETD)^4 - T_{REF}^4], \quad (7)$$

where $P(T)$ is the incident power falling on the senor surface when the blackbody works at a temperature T. The value of NETD calculated for a reference temperature of 300 K is approximately 90 *m*K. This value is comparable to some recent results of a-Si resistive bolometers [11] and PZT pyroelectric sensors [3]. It is believed NETD can be further reduced when some parameters such as the geometrical shape of the microbridge and the thermal behavior of the a-Si TFT are optimized.

5. CONCLUSION

We have demonstrated an a-Si TFT-based uncooled infrared sensor using MEMS

micromachined sensors with the smart electronics.

Theoretical analysis shows that both the carrier mobility shift and the threshold voltage shift of the a-Si TFT contribute to the large of temperature coefficient of the channel current. Experimental results show that the a-Si TFT in the saturation region has a TCC value of 3.8-6.0 %/K which makes it a promising candidate for the sensitive elements of IR sensors.

The fabrication processing of the sensor is compatible with the standard IC processing, which enables to reduce the costs of IR sensors.

Optical measurements show a responsivity of 40.8 *k*V/W, a thermal response time of 5.5 *m*s and a NETD of 90 *m*K are achieved.

ACKNOWLEDGEMENTS

The authors would like to acknowledge the technical assistance of Mr Wanjie Zhang and Prof. Yuqin Gu. The work was supported by the "985" Foundation of Tsinghua University and the National Natural Science Foundation of China (No.59995550-1).

REFERENCES

[1] S.Sedky, P.Fiorini, K.Baert, L.Hermans, et al., "Characterization and Optimization of infrared poly SiGe bolometers," IEEE Trans. Electron Devices, 46, (1999) 675-681.

[2] M.Noda, K.Hashimoto, R.Kubo, et al., "A new type of dielectric bolometer mode of detector pixel using ferroelectrics thin film capacitors for infrared image sensor," Sensors and Actuators A, 77, (1999) 39-44.

[3] T.D.Binnie, H.J.Weller, Z.He, et al., "An integrated 16×16 PVDF pyroelectric sensor array", IEEE Tran. Ultrabond., Ferroelect., Freq., Contr., 47(6), (2000) 1413-1420.

[4] D.O.Andrew and D.W.Kensall, "A 1024-element bulk-micromachined thermopile infrared imaging array," Sensors and Actuators A, 73, (1999) 222-231.

[5] Y.Zhang, M.Mao, R.Horowitz, et al., "Orthomechanical uncooled infrared imaging system: design, microfabrication, and performance", Journal of Microelectromechanical Systems, 11(2), (2002) 136-146.

[6] J.R.Vig, R.L.Filler, and Y.Kim, "Uncooled IR imaging array based on quartz microresonators", Journal of Microelectromechanical Systems, 5(2), (1996) 131-137.

[7] A. Jahanzeb, C.M.Travers, Z.C.Butler, et al., "A semiconductor bacto microbolometer for room temperature IR imaging", IEEE Trans. Electron Devices, 44(10), (1997) 1795-1801.

[8] R.A.Wood, "High-performance infrared thermal imaging with monolithic silicon focal planes operating at room temperature," IEDM Tech. Dig., (1993) 175-177

[9] R.A.Street, "Technology and applications of amorphous silicon," New York: Springer, (2000) 43-45.

[10] E.Ibarra, M.Clement, L.V.Herrera, et al., "IR uncooled bolometers based on amorphous GexSi1-xOy on silicon micromachined structures," Journal of Microelectromechanical Systems, 11(4), (2002) 322-329.

[11] J.L.Tissot, "320×240 microbolometer uncooled IRFPA development," SPIE, Infrared technology and application XXVI, 4130, (2000) 473-479.